THE JOURNAL OF PHYSICAL CHEMISTRY C

pubs.acs.org/JPCC

Article

Integrated Experimental and Theoretical Approach for Efficient Design and Synthesis of Gold-Based Double Halide Perovskites

Beata Bajorowicz, Alicja Mikolajczyk, Henry P. Pinto, Magdalena Miodyńska, Wojciech Lisowski, Tomasz Klimczuk, Ifat Kaplan-Ashiri, Miri Kazes, Dan Oron,* and Adriana Zaleska-Medynska*

Cite This: *J. Phys. Chem. C* 2020, 124, 26769–26779

Read Online

ACCESS | Metrics & More | Article Recommendations | Supporting Information

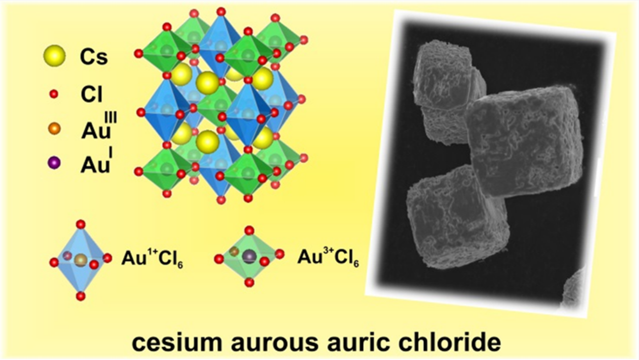

ABSTRACT: Applied cutting-edge electronic structure and phonon simulations provide a reliable knowledge about the stability of perovskite structures and their electronic properties, which are crucial for design of effective nanomaterials. Gold is one of the exceptional elements, which can exist both as a monovalent and a trivalent ion in the B site of a double perovskite such as $A_2B^{I}B^{III}X_6$. However, until now, electronic properties of $Cs_2Au^{I}Au^{III}X_6$ have not been sufficiently explored and this material was never synthesized using Au^{1+} and Au^{3+} precursors in the preparation route. Here, computational simulations combined with an experimental study provide new insight into the properties and synthesis route of $Cs_2Au^{I}Au^{III}X_6$ (X = Cl, Br, and I) perovskites. First-principles calculations reveal that tetragonal $Cs_2Au^{I}Au^{III}X_6$ (X = I, Br, Cl) molecules present a band gap of 1.10, 1.15, and 1.40 eV, respectively. Application of novel approaches in the simulations of the VB-XPS for $Cs_2Au^{I}Au^{III}Cl_6$ allows replication of the observed spectrum and provides strong evidence of the reliability of the obtained results for the other perovskites $Cs_2Au^{I}Au^{III}X_6$, X = Br, I. Following theoretical findings, a one-step preparation route of the $Cs_2Au^{I}Au^{III}Cl_6$ is developed using a combination of monovalent and trivalent gold precursors at a relatively low temperature. It should be emphasized that this is the first synthesis of this material at low temperatures, allowing for obtaining highly crystalline $Cs_2Au_2Cl_6$ particles with controlled morphology and without gold impurities. The band gap of synthesized $Cs_2Au^{I}Au^{III}Cl_6$ is extended into the NIR spectral range, where most other double perovskites are limited to higher energies, limiting their usage in single junction solar cells or in photocatalysis. The as-synthesized $Cs_2Au^{I}Au^{III}Cl_6$ exhibits high efficiency in a photocatalytic toluene degradation reaction under visible light irradiation. The developed approach provides information necessary for structure manipulation at the early stage of its synthesis and offers a new and useful guidance for design of novel improved lead-free inorganic halide perovskite with interesting optical and photocatalytic properties.

■ INTRODUCTION

Halide perovskites possess the chemical formula ABX_3 (where A and B are large electropositive cations and X is an anion). Recently, halide perovskites (where X = Cl^-, Br^-, and I^-)—both organic–inorganic hybrids and fully inorganic lead-based (e.g., $CsPbX_3$), have been extensively explored to appraise their potential in photovoltaic applications.[1−5] The toxicity of lead (which is commonly used in halide perovskite-based devices) and the relative instability of divalent tin have led to the search for alternative analogous materials including a variety of double halide perovskites.

Double perovskites represent the structure employing two different types of cations, the formulas of which are $AA'B_2X_6$ or $A_2BB'X_6$.[6] In most recently studied double perovskites, the toxic divalent Pb^{2+} ions are replaced by one monovalent and one trivalent ion, maintaining the total number of valence electrons. Experimentally and theoretically, it was revealed that a wide group of lead-free double perovskites, keeping one monovalent and one trivalent cation at the B site, could exist, such as $Cs_2AgBiCl_6$, Cs_2AgBiI_6, $Cs_2CuSbCl_6$, $Cs_2CuSbBr_6$, $Cs_2CuBiBr_6$, $Cs_2AgSbBr_6$, Cs_2AgSbI_6, $Cs_2AuSbCl_6$, $Cs_2AuBiCl_6$, $Cs_2AuBiBr_6$ $Cs_2InSbCl_6$, $Cs_2InBiCl_6$, $Cs_2TlSbBr_6$, Cs_2TlSbI_6, and $Cs_2TlBiBr_6$; nonetheless, most of them have not been synthesized today.[7] Moreover, a replacement of the divalent lead cation can be realized by a mixed-valence approach in which single-metal cations exist in mono- and

Received: August 26, 2020
Revised: November 7, 2020
Published: November 19, 2020

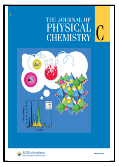

https://dx.doi.org/10.1021/acs.jpcc.0c07782
J. Phys. Chem. C 2020, 124, 26769−26779

trivalent forms,[8] which was reported for toxic thallium[9] and promising gold[10,11] halide perovskites.

Cesium aurous auric chloride, studied here, was obtained for the first time by Wells in 1922 by heating of aurous chloride with cesium chloride dissolved in hydrochloric acid substrate in hydrochloric acid,[12] while its crystal structure was determined by Pauling and Elliot in 1938.[11] The observed extraordinarily black color of the sample implied the presence of gold in two valence states. Finally, it was revealed that the unit cell of this perovskite comprises elongated octahedra with Au(III) and compressed octahedra with Au(l), which form a three-dimensional metal−halogen framework.[13−15] Several different methods for gold-based double perovskites synthesis have been proposed. $Cs_2Au_2Cl_6$ was prepared by high-temperature decomposition of $CsAuCl_4$ salt under nitrogen flow,[16] while single crystals of $Cs_2Au^{I}Au^{III}I_6$ and $Cs_2Au^{I}Au^{III}Br_6$ were obtained by slowly cooling mixtures of CsI, Au and I_2 or CsBr, Au and liquid bromide, respectively.[17] These synthesis methods allowed for obtaining $Cs_2Au_2Cl_6$ and some gold crystals impurities.[14] A neglected area in the field of gold-based double perovskites is a systematic exploration of $Cs_2Au^{I}Au^{III}X_6$ perovskite ($X = Cl^-$, Br^-, and I^-) band gap structure as well as a new synthesis route employing a combination of Au^{1+} and Au^{3+} precursors (which are presently available).

Here, we present a combination of improved density functional theory (DFT) calculations and an experimental study of the electronic structure of $Cs_2Au_2X_6$ (X = Cl, Br, I) perovskites and a novel preparation route of perovskite-like $Cs_2Au_2Cl_6$ using two different gold precursors under solvothermal or reflux conditions. Application of spin−orbit corrections allows explaining the observed VB-XPS spectrum and assigns accurately the nature of the observed peaks. Optimization of synthesis parameters allowed for obtaining highly crystalline $Cs_2Au_2Cl_6$ particles with controlled morphology and without gold impurities. Moreover, physicochemical characterization involving optical and surface properties and the crystal structure analysis of $Cs_2Au_2Cl_6$ was performed and supported by DFT calculations. Finally, the application of perovskite-type cesium gold chloride in a photocatalytic toluene degradation reaction was proposed for the first time.

■ METHODS

Preparation of $Cs_2Au_2Cl_6$. In brief, solid CsCl, $AuCl_3$, and AuCl in appropriate molar proportions were mixed with HCl (10 mL) in a round-bottom flask for 15 min. The precursor solution was then heated to 115 °C to form a clear solution under reflux conditions or transferred into a Teflon-lined stainless steel autoclave at 115 °C for 0.5 h. After that, in the case of heating under reflux, 10 vol % DMSO for HCl was added into the hot precursor solution, and the black $Cs_2Au_2Cl_6$ crystals were precipitated from the precursor solution immediately. The crystals obtained both under reflux and solvothermal conditions were filtered when the solution was hot and subsequently washed with water and ethanol several times. Finally, they were dried in an oven at 70 °C for 12 h.

Characterization. X-ray photoelectron spectroscopic (XPS) measurements were performed using a PHI 5000 VersaProbe (ULVAC-PHI) spectrometer with monochromatic Al Kα radiation ($h\nu$ = 1486.6 eV). The high-resolution (HR) XPS spectra were collected with a hemispherical analyzer at a pass energy of 23.5 eV, energy step size of 0.1 eV, and photoelectron take off angle of 45° with respect to the surface plane. The binding energy (BE) scale of all detected spectra was referenced to the carbon (C−C) signal of 284.8 eV in the C 1s spectrum. Powder X-ray diffraction (pXRD) was used to confirm the crystal structure and calculate the lattice parameters of double perovskites $Cs_2Au_2Cl_6$. The pXRD patterns were collected using a Bruker D2 Phaser 2nd generation diffractometer equipped with a Cu Kα radiation source (λ = 1.54056 Å) and a LynxEye XE-T detector. The lattice parameters were analyzed using the LeBail profile method using High Score Plus software.

The morphology of $Cs_2Au_2Cl_6$ nanoparticles was observed by high-resolution SEM (Zeiss GeminiSEM 500), using an SE2 detector at 20 kV and a 20 μm aperture in analytic gun mode. Further analyses of selected regions of interest (ROIs) were performed by EDS (energy-dispersive X-ray spectroscopy) and CL (cathodoluminescnence) both installed on the SEM using the same parameters described for imaging. The EDS measurements were performed using a 60 mm SDD (silicon drift detector) from Bruker (Quntax6−60), a hyper map of the desired ROI was collected, and the elements were mapped according to the spectral information. Using this method, different features or morphologies that appeared in the image could be chemically identified, both qualitatively and quantitatively. Quantification was performed by a P/B-ZAF standardless analysis method. To collect SEM-CL spectra, we used a Gatan MonoCL Elite system equipped with a retractable diamond-turned mirror. The collected light was first imaged in panchromatic mode using a high-sensitivity PMT (photomultiplier tube) with a spectral range of 160−930 nm. For spectral information, the collected light was directed to a monochromator and a charge-coupled device (CCD) for parallel spectroscopy. The spectral range was set to 300−800 nm with a band pass of 20 or 40 nm by choosing the 150 lines/mm grating centered on 550 nm and 1 or 2 mm entrance slit. CL was collected for several points (single pixels) that were marked on the SEM image, with an exposure time of 2 s per pixel.

Measurement of Photocatalytic Activity. The photocatalytic activity of $Cs_2Au_2Cl_6$ samples was determined in the toluene degradation process. The photocatalytic activity tests were performed in a flat stainless steel reactor (V = 30 cm^3) equipped with a quartz window, two valves, and a septa. As an irradiation source, an array of 25 UV LEDs (λ_{max} = 375 nm) or 25 Vis LEDs (λ_{max} = 415 nm) was used. In a typical measurement, the semiconductor powder (about 0.1 g) was suspended in a small amount of water and loaded as a thick film on a glass plate (3 cm × 3 cm) using a painting technique. The obtained semiconductor-coated support was dried and then placed at the bottom side of the photoreactor followed by closing the reactor with a quartz window. The gaseous mixture from a cylinder was passed through the reactor space for 1 min. The concentration of toluene in a gas mixture was about 200 ppm. After closing the valves, the reactor was kept in the dark for 30 min to reach adsorption equilibrium. A reference sample was taken just before starting irradiation. To estimate toluene concentration, the samples were taken every 20 min for 60 min of irradiation. The analysis of toluene concentration in the gas phase was carried out using a Perkin Elmer Clarus 500 GC (Perkin Elmer, Waltham, USA) equipped with a 30 m × 0.25 mm Elite-5 MS capillary column (0.25 μm film thickness) and a flame ionization detector (FID). The samples (200 μL) were injected using a gas-tight syringe. Helium was used as a carrier gas at a flow rate of 1 mL·min^{-1}.

Computational Details. Density functional theory (DFT) calculations were performed using the plane wave basis Vienna *ab initio* simulation package (VASP).[18,19] Core electrons are described by projected augmented wave (PAW) potentials,[20] where the potential for the cesium atom was generated in the electron configuration [Kr,4d10]$5s^2 5p^6 6s^1$, that for gold was in [Kr,$4f^{14}$,$4d^{10}$]$5s^2 5p^6 6s^1 5d^{10}$, that for bromine was in [Ar,$3d^{10}$]-$4s^2 4p^5$, that for chlorine was in [Ne]$3s^2 3p^5$, and that for iodine was in [Kr, $4d^{10}$]$5s^2 5p^5$, where square brackets denote the core electron configurations. The optimal bulk crystal structures of $Cs_2Au_2X_6$ (X = Br, Cl, I) were computed using strongly constrained and appropriately normed (SCAN) meta-generalized gradient approximation (meta-GGA) as implemented in VASP.[21,22] Using a kinetic cutoff energy of 650 eV and appropriate Γ-centered Monkhorst−Pack *k*-point meshes with separation of 0.035 $Å^{-1}$, we converge the total energy to <1 meV/atom. Finally, the ionic optimizations were performed until all the forces were below 0.01 $eVÅ^{-1}$. Accurate electronic structure properties were computed using SCAN optimal crystal structures and applying the hybrid Hartree−Fock DFT functional Heyd−Scuseria−Ernzerhof HSE06[23,24] including spin−orbit corrections (SOC): HSE06 + SOC. It is important to stress that the SCAN functional has been proven to be superior in the prediction of crystal structures and formation energies: in fact, SCAN accurately predicts diverse kinds of bondings,[25] and it performs better than PBE when applied to semiconductors,[25] structural distortions in ferroelectrics,[26] critical pressures for phase transitions in semiconductors,[27] and structural predictions for solids including transition-metal oxides,[28] to name some of the advantages. Furthermore, SCAN is also found to improve the prediction of crystal structures and formation energies compared to hybrid functionals.[25,29] For these reasons, we selected SCAN to predict the crystal structure of the systems we study here. Then, the electronic structure of the lattice previously optimized using SCAN is computed using HSE06 + SOC; this level of calculation considers accurate lattice predictions with band gap estimations that includes spin−orbit corrections.

Table S1 displays the SCAN prediction of the bulk properties of the $Cs_2Au_2X_6$ (X = Br, Cl, I) perovskites including the corresponding computed HSE06 + SOC band gaps. To further explore and confirm the mechanical stability of the $Cs_2Au_2X_6$ perovskites with *I*4/*mmm* symmetry, the phonon band structure was computed using SCAN and the frozen phonon method as implemented in the phonopy code.[30] A supercell 2 × 2 × 1 constructed from the unit cell of the $Cs_2Au_2X_6$ (X = Br, Cl, I) perovskites with *I*4/*mmm* symmetry and 2 × 2 × 2 *k*-point mesh was necessary to get convergent results.

■ RESULTS AND DISCUSSION

The first step toward theoretical predictions of the electronic structure of perovskites is the prediction of the stability of double perovskite $Cs_2Au^IAu^{III}X_6$ (X = Cl, Br, I) using the well-known Goldschmidt tolerance factor,[31] $t = (r_A + r_X)/\sqrt{2}(r_B + r_X)$, initially developed to predict perovskite compounds ABX_3. This factor has the advantage of predicting new perovskites by knowing only the effective ionic radii[32] r_i of A, B, and X ions. For double perovskites $A_2BB'X_6$, the *t* factor can be extended using the mean value of r_i for B and B′ ions. According to Goldschmidt's work, stability is found if $0.825 < t < 1.059$ and $r_A > r_B$ by definition. Estimation of *t* for $Cs_2Au^IAu^{III}X_6$ with X = Cl, Br, and I is 0.843, 0.836, and 0.827, respectively; this result suggests the stability of this kind of double perovskite. It is interesting to take into account a recent work by Bartel et al.[33] where a novel tolerance factor for perovskites $\tau = (r_X/r_B) - n_A[n_A - (r_A/r_B)/\ln(r_A/r_B)]$, where n_A is the oxidation state of A (in our case A = Cs, then +1), is proposed. Stability is predicted if $\tau < 4.18$. The computed tolerance τ for $Cs_2Au^IAu^{III}X_6$ with X = Cl, Br, and I yields 4.31, 4.45, and 4.67, respectively, suggesting that these double perovskites are unstable in contrast to Goldschmidt tolerance factor prediction. This discrepancy of stability as predicted by *t* and τ factors could be related to the nature of these factors: *t* is derived from geometric constraints that allow assessment if a possible structure is likely to form; τ is a data-driven approach trained considering ABX_3 compounds. According to the work of Bartel et al.,[33] τ is more robust in predicting perovskite compounds since it also includes the octahedral factor (r_X/r_B) and the oxidation state of A; nevertheless, $Cs_2Au^IAu^{III}X_6$ (X = Cl, Br, and I) seems to contradict the stability as predicted by *t*. High-accuracy DFT calculations provide a water-proof method to elucidate what should be expected experimentally, and our simulation of phononic properties displayed in Figure 2 is in agreement with the Goldschmidt tolerance factor. This interesting discrepancy between *t* and τ found in these double perovskites suggests the importance of using descriptor-based approaches with the support of DFT calculations for a reliable prediction of compound stability. Finally, it is important to mention that in the literature, we found other high-accuracy models to predict stability using a random forest of decision trees,[34] kernel support vector machines,[35] or gradient boosted decision trees;[36] unfortunately in these approaches, the descriptors are not well documented making them difficult to implement.

We applied DFT to investigate mixed-valence halide $Cs_2Au^IAu^{III}X_6$ perovskites with potentially superior photocatalytic performance. In the first step, we have performed DFT calculations in order to investigate the influence of the choice of halide (X = Cl, Br, I) and the crystal phase on the electronic structure properties of different configurations of mixed halide $Cs_2Au^IAu^{III}X_6$ perovskites (Figure 1).

To clarify both the impact of phase and the influence of halide on property changes of $Cs_2Au_2X_6$ perovskites, we used

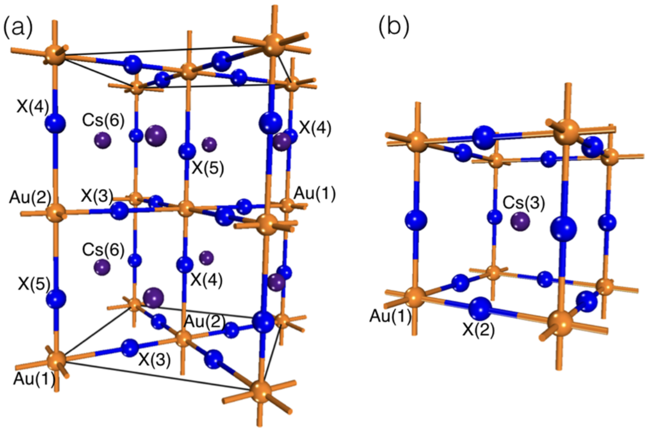

Figure 1. Unit cell of simulated crystal structures of $Cs_2Au^IAu^{III}X_6$ perovskites with symmetry (a) *I*4/*mmm* (no. 139) and (b) *Pm*-3*m* (no. 221). In these images, the yellow, blue, and violet spheres represent Au, X, and Cs, respectively. The labels on the atom sites are in correspondence to Table S1.

state-of-the-art DFT methods that include spin−orbit corrections (SOCs) (see methodology description and the Supporting Information). To evaluate the crystallographic stability of the material in the halide $Cs_2Au^IAu^{III}X_6$ perovskites, the energy difference between tetragonal and cubic structures ($\Delta E_{T\text{-}C}$ (eV/fu)) was investigated (Table 1 and Figure S1).

Table 1. Optimized Lattice Constants and Calculated Properties of $Cs_2Au^IAu^{III}X_6$ vs Experimentally Obtained data[37] for X = Cl[b]

space group	property	X = Br	X = I	X = Cl	exp. X = Cl
symmetry	V_0 (Å^3)	688.75	833.28	604.72	612.28
I4/mmm	$a = b$ (Å)	7.769	8.285	7.447	7.5
no. 139	c (Å)	11.412	12.141	10.905	10.884
tetragonal	B_0 (GPa)	15.99	12.77	16.57	15
	E_g (eV)	0.81 (1.15)	0.85 (1.10)	0.97 (1.40)	
symmetry	V_0 (Å^3)	155.62	188.65	134.10	
Pm-3m	a (Å)	5.379	5.735	5.119	
no. 221	B_0 (GPa)	36.59	31.06	44.31	
cubic	E_g (eV)	0.0	0.0	0.0	
	$\Delta E_{T\text{-}C}$ (eV/fu)[a]	−0.61	−0.60	−0.75	

[a] fu = $Cs_2Au_2X_6$, (X = Br, I, Cl).

The analysis of investigated halide perovskites indicated that in all the cases, the most stable phase is the tetragonal perovskite with the space group *I4/mmm* (no. 139), where the energy difference between the two phases $\Delta E_{T\text{-}C}$ decreases in the order I > Br > Cl (Table 1). Interestingly, the unit cell volume (V_0) decreases in the same order (i.e., I > Br > Cl, Figure 2 and Table 1). The obtained results of simulated crystal structure for X = Cl are in agreement with experimental data presented for the first time in 1998 by Matsushita et al. (Table 1).[37]

[b]In the case of $Cs_2Au^IAu^{III}Cl_6$, a relation between computed EOS for both phases predicts a pressure-induced phase transition of ∼11.4 GPa that agrees with the measured 12 GPa[37] (cf. Figure S1). The values correspond to the optimal volume at zero pressure (V_0), the predicted unit cell lattice constants (a, b, c), the bulk modulus (B_0), and the band gap (E_g). The values of E_g show both the computed values using SCAN and HSE06 + SOC within parentheses.

To further check the structural stability of the $Cs_2Au^IAu^{III}X_6$ perovskites with symmetry *I4/mmm*, we computed the phonon band structure and partial density of states (PDOS), and the results are displayed in Figure 2. The phonon calculations show no negative frequencies within the Brillouin zone, meaning that $Cs_2Au^IAu^{III}X_6$ perovskites with X = Br, I, and Cl and symmetry *I4/mmm* are stable. It is important to mention that these phonon calculations have not included dipole−dipole interaction corrections as it is expected that the final outcome will not affect the dispersion of the acoustic phonons.

Using the SCAN predicted atomic structure of $Cs_2Au^IAu^{III}X_6$ perovskites with symmetry *I4/mmm* (no. 139), we apply HSE06 + SOC to investigate the electronic structure. The outcome of the calculations shows that all the systems have an indirect band gap, where the maximum (minimum) of the valence (conduction) band is within the Σ−Γ path (cf. insets in Figure 3). The composition of the upper valence band is composed of two peaks located in the lower part with character Cs 5p states; the middle region has a main contribution of Au 5d states with some contributions of Br 4p (Figure 3a), I 5p (Figure 3b), and Cl-3p (Figure 3c); in all the PDOSs, we observe a main peak at approximately −2 eV that has a Br 4p, I 5p, or Cl 3p character; (cf. Figure 3a−c). The lowest conduction band as displayed in the computed band structure figures presents corresponding peaks in the PDOS within the range of 1.0 to 2.5 eV, and these peaks are

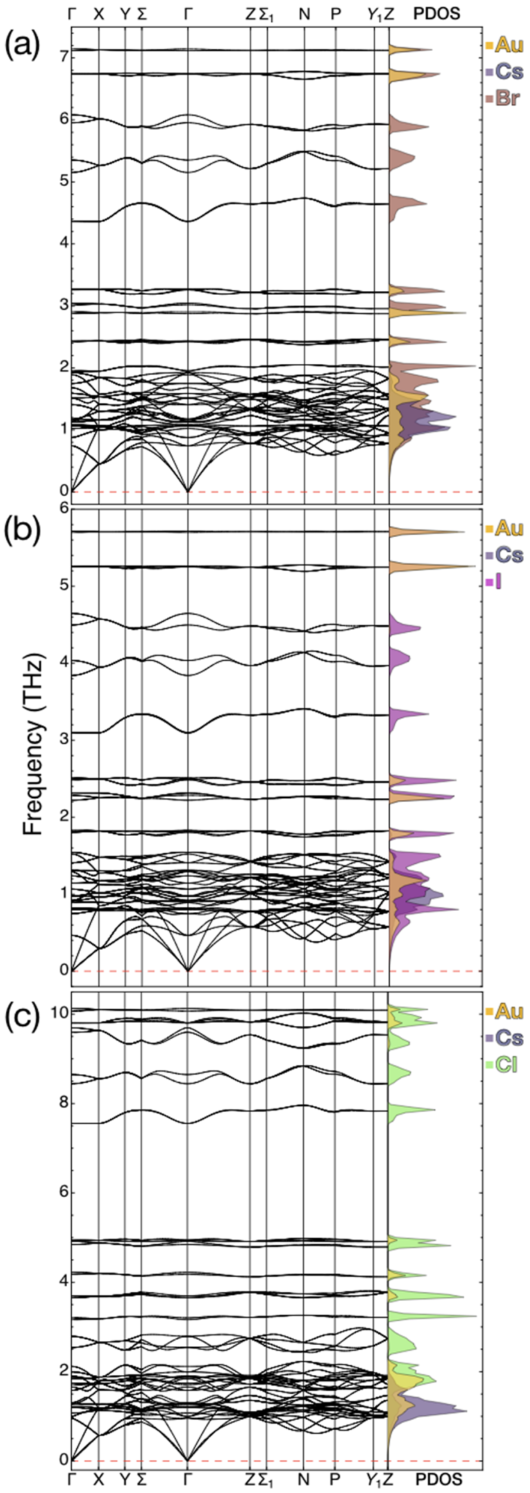

Figure 2. DFT-SCAN computed phonon band structure and corresponding PDOS for $Cs_2Au^IAu^{III}X_6$ with symmetry *I4/mmm* for (a) X = Br, (b) X = I, and (c) X = Cl. The results show a stable phase with no negative frequencies for all the different halides.

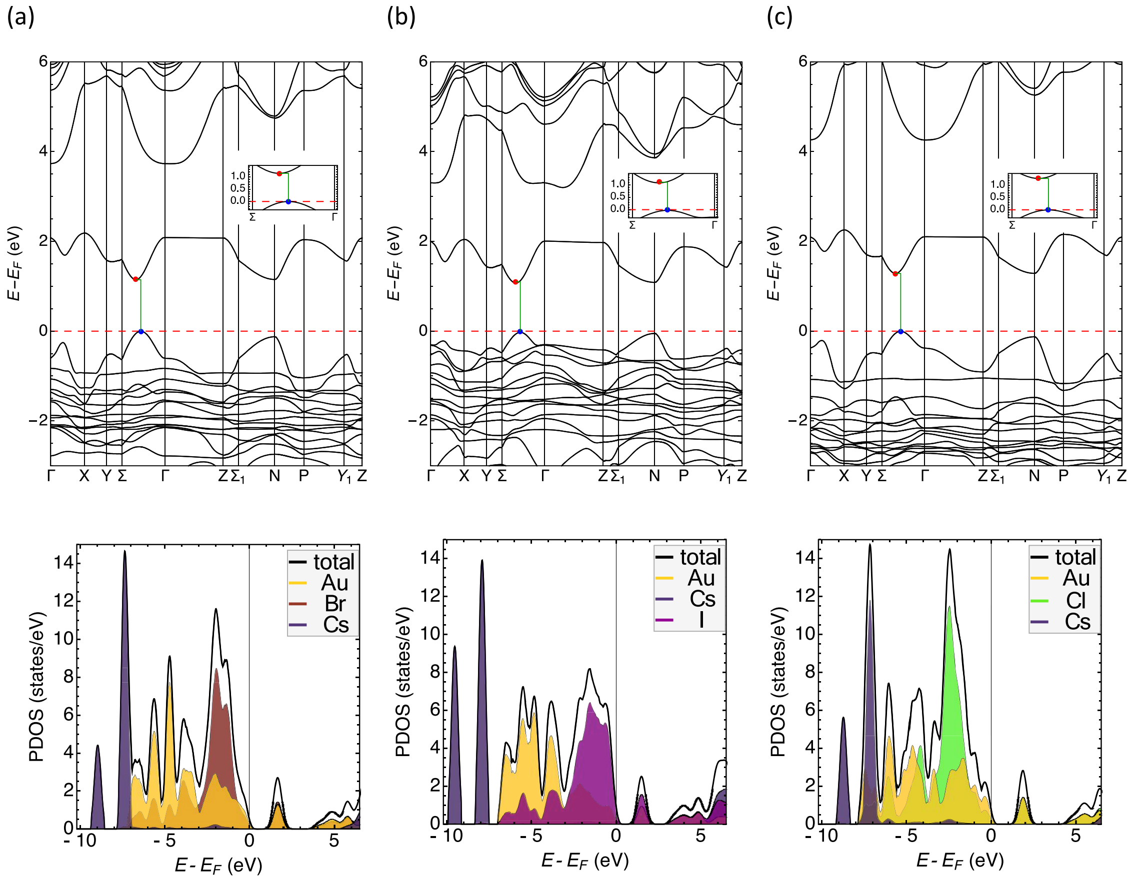

Figure 3. HSE06 + SOC-computed band structure and partial density of electronic states of $Cs_2Au^IAu^{III}X_6$ with symmetry *I*4/*mmm* for (a) X = Br, (b) X = I, and (c) X = Cl. The blue (red) points in the computed band structures locates the valence (conduction) band maximum (minimum); we observe a small shift along the wave vector path Σ−Γ of both points, and a close up of these sections are displayed in the corresponding insets.

Table 2. Sample Label, Preparation Conditions, and Structural Properties of $Cs_2Au_2Cl_6$

	Molar ratio			lattice parameter		
sample label	$(AuCl + AuCl_3)/CsCl$	HCl concentration (%)	Type of heating	a (Å)	c (Å)	intensity ratio *I*(220)/*I*(112)
$Cs_2Au_2Cl_6$_1	1:2	38	reflux	7.50459(7)	10.8928(1)	0.95
$Cs_2Au_2Cl_6$_2	1:2	19	reflux	7.4964(2)	10.8845(3)	2.00
$Cs_2Au_2Cl_6$_3	1:2	38	solvothermal	7.50357(7)	10.8899(1)	0.37
$Cs_2Au_2Cl_6$_4	1:1	38	reflux	7.4981(2)	10.8818(3)	0.30
$Cs_2Au_2Cl_6$_5	2:1	38	reflux	7.50665(5)	10.89129(8)	0.74
$Cs_2Au_2Cl_6$_6	1:1	19	reflux	7.4958(1)	10.8885(2)	0.43
$Cs_2Au_2Cl_6$_7	2:1	19	reflux	7.50256(7)	10.8917(1)	0.53
$Cs_2Au_2Cl_6$_8	1:2	19	solvothermal	7.50415(5)	10.8890(1)	0.40

formed by Au 5d + Br 4p (Figure 3a), Au 5d + I 5p (Figure 3b), and Au 5d + Cl 3p (Figure 3c) states.

While the HSE06 + SOC-calculated electronic band gaps for $Cs_2Au^IAu^{III}I_6$, $Cs_2Au^IAu^{III}Br_6$, and $Cs_2Au^IAu^{III}Cl_6$ perovskites are equal to 1.10, 1.15, and 1.40 eV, respectively (Figure 3); these results are in good agreement with a recent calculation using HSE06 + G_0W_0 where indirect band gaps of $Cs_2Au^IAu^{III}X_6$ of 1.45, 1.61, and 2.08 eV for X = I, Br, and Cl, respectively, are also reported.[38] The fact that $Cs_2Au^IAu^{III}I_6$, $Cs_2Au^IAu^{III}Br_6$, and $Cs_2Au^IAu^{III}Cl_6$ perovskites possesses an indirect band gap suggests that the halide perovskites studied here may potentially exhibit very good light harvesting properties.

Following these theoretical and numerical findings, a novel preparation route of $Cs_2Au_2Cl_6$ using a combination of monovalent and trivalent gold precursors was developed. The perovskite-like $Cs_2Au_2Cl_6$ was obtained by a simple one-step method under solvothermal or reflux conditions at a relatively low temperature (see experimental details). The change of synthesis parameters such as the molar ratio of gold precursors, solvent concentration, and type of heating (Table 2) determined the physicochemical properties of the obtained samples.

The room-temperature pXRD patterns for samples $Cs_2Au_2Cl_6$_2 and $Cs_2Au_2Cl_6$_5 (see Table 3) are presented in the upper and lower panel, respectively (Figure 4). The data points are represented by black circles, the red line is the profile (LeBail) fit. The pXRD analysis of all tested samples confirms the tetragonal structure of dicesium gold chloride as reported in refs 37 and 39. All the diffraction peaks correspond to the tetragonal *I*4/*mmm* (no. 139) structure, and the only impurity seen for some of the samples is elemental gold. The

https://dx.doi.org/10.1021/acs.jpcc.0c07782
J. Phys. Chem. C 2020, 124, 26769−26779

Table 3. Elemental Composition (at. %) and Chemical State of Au at the Surface Layer of $Cs_2Au_2Cl_6$, Evaluated by XPS Analysis

						chemical state of Au (%)			
						Au $4f_{7/2}$			
	elemental composition (at. %)					Au(0)	Au(1+)	Au(3+)	
sample label	Cs	Au	Cl	O + C + S	Cs/Au	84.0 ± 0.1 eV	84.6 ± 0.1 eV	$Cs_2Au_2Cl_6$ 86.3 ± 0.2 eV	$Au-(OH)_3$ 87.5 ± 0.1 eV
$Cs_2Au_2Cl_6$_1	19.18	17.44	39.26	24.12	1.10	10.8	56.7	25.7	6.9
$Cs_2Au_2Cl_6$_2	17.75	15.67	41.10	25.48	1.13	0.4	59.4	23.3	16.9
$Cs_2Au_2Cl_6$_3	16.58	14.91	37.58	30.93	1.11	14.4	45.1	29.8	10.7
$Cs_2Au_2Cl_6$_4	19.12	15.99	42.94	21.95	1.19	1.1	55.1	25.4	18.4
$Cs_2Au_2Cl_6$_5	7.48	10.79	26.79	54.94	0.69	2.6	66.9	17.4	13.1
$Cs_2Au_2Cl_6$_6	18.21	15.80	40.89	25.10	1.15	0.7	64.9	22.7	11.7
$Cs_2Au_2Cl_6$_7	19.94	16.69	43.42	19.95	1.19	1.3	59.8	24.3	14.6
$Cs_2Au_2Cl_6$_8	19.70	16.71	40.23	23.36	1.18	10.3	57.9	24.9	6.9

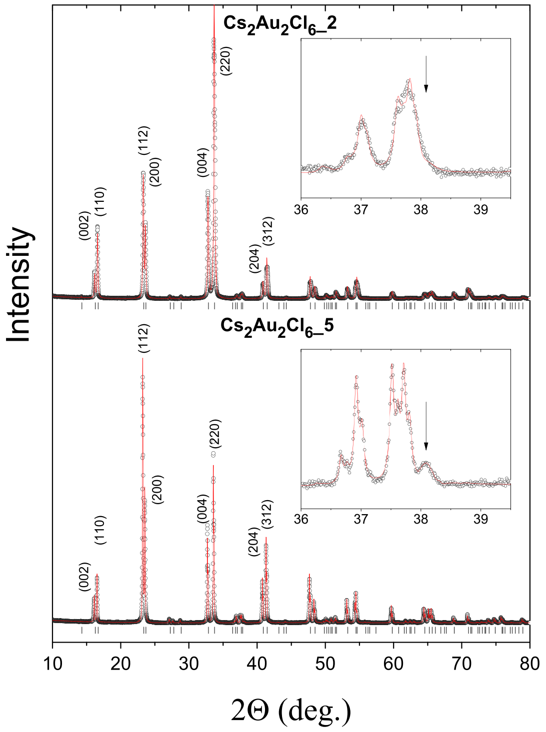

Figure 4. Powder X-ray diffraction pattern (pXRD) for sample $Cs_2Au_2Cl_6$_2 (upper panel) and $Cs_2Au_2Cl_6$_5 (lower panel). The red line shows the profile LeBail fit to the experimental data (black points). Tick marks are positions of the tetragonal Cs_2AuCl_6 Bragg reflections. The inset shows part of the pXRD in which the strongest gold reflection (marked by an arrow) is observed.

strongest XRD reflection of gold is expected at around 38° and is marked by an arrow (Figure 4 and Figure S2). The presence of some Au impurity peaks detected by XRD analysis is probably due to the use of the Au^I (AuCl) precursor, which can disproportionate into Au^{III} and Au^0 during synthesis of $Cs_2Au_2Cl_6$. Ghosh et al.[40] observed formation of both metallic gold and $(CH_3NH_3)_2Au_2I_6$ during synthesis of double perovskite because of disproportionation of the Au^I starting material. Meanwhile, using only Au^{III} salts to prepare $MA_2Au_2Br_6$ resulted in a pure phase of perovskite.[40] Moreover, it can be seen that XRD analysis revealed the absence or much smaller gold impurity peaks for $Cs_2Au_2Cl_6$ samples obtained via the reflux method than that prepared via a solvothermal route. It may be suggested that a close system and pressure generated during solvothermal process favor formation of a higher amount of gold particles as compared with the open reflux system.

The lattice parameters obtained from the LeBail method are gathered in Table 3. The values of *a* and *c* do not change significantly in the series and are in good agreement with the reported literature.[37,39] An interesting feature is a preferential orientation effect observed for some of the samples. For a powderized sample with unoriented grains, the expected intensity ratio $I(220)/I(112)$ is 0.34, whereas the observed $I(220)/I(112)$ reaches 0.95 for $Cs_2Au_2Cl_6$_1 and 2 for $Cs_2Au_2Cl_6$_2.

The elemental composition (at. %) detected by XPS at the surface layer of $Cs_2Au_2Cl_6$ samples is specified in Table 3. The relative contents of Cs, Au, and Cl confirm the successful preparation of mixed-valence $Cs_2Au_2Cl_6$ complexes. The average value of the Cs/Au ratio evaluated for all samples is close to unity (1.09 ± 0.16). A relatively large amount of carbon, sulfur, and oxygen (Table 3) probably originates from the other compounds remaining after preparation. In order to characterize the mixed-valence states of Au in the synthesized $Cs_2Au_2Cl_6$ samples, we analyzed both the core-level Au 4f spectra (presented in Figure 5a) and valence band (VB) spectra (shown in Figure 5b). The Au 4f curve-fitting spectra of exemplary samples, $Cs_2Au_2Cl_6$_1 and $Cs_2Au_2Cl_6$_3, are presented in Figure 5c. Au 4f spectra of both samples reveal four oxidation states of Au, formed by $4f_{7/2}$ and $4f_{5/2}$ spin−orbit splitting components, with an intensity ratio of 4:3 and separated by 3.67 eV.[41] The first state, at a binding energy (BE) of $Au4f_{7/2}$ close to 84.0 eV, is attributed to Au(0),[41] and the second one (Au $4f_{7/2}$ at 84.6 eV) is to Au(1+) components.[42,43] The next two states of Au (Au $4f_{7/2}$ at 86.3 and 87.5 eV) are identified as Au(3+) components of $Cs_2Au_2Cl_6$[42,43] and Au(3+) hydroxide,[44] respectively.

The valence band (VB) XPS spectra, taken for all $Cs_2Au_2Cl_6$ samples, show a similar shape. However, small BE shifts are observed for samples obtained both under reflux and solvothermal conditions. These chemical shifts can be assigned to various mixed-valence states of Au contribution and can also be a result of surface modification by contaminants remaining after synthesis. The measured VB-XPS spectrum was compared with the simulated XPS at the level of HSE06 + SOC calculation. Figure 6 displays a comparison between the observed spectrum for $Cs_2Au_2Cl_6$ and the HSE06 + SOC simulated XPS spectrum at $h\nu = 1486.6$ eV (cf. Figure 6a). The peaks of the simulated spectrum are in good agreement with

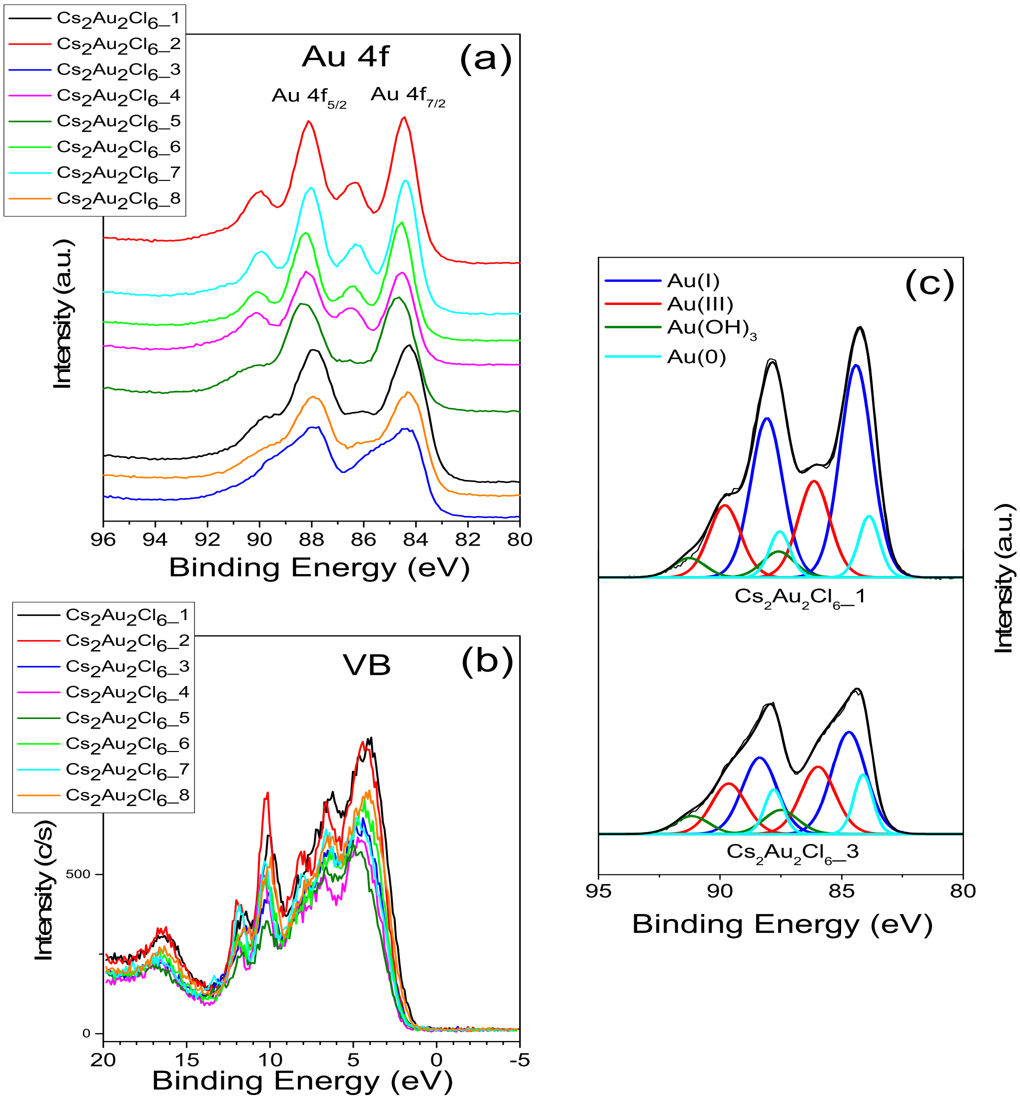

Figure 5. (a) Au 4f XPS spectra of all $Cs_2Au_2Cl_6$ samples, (b) valence band (VB) XPS spectra, and (c) Au 4f curve-fitting spectra of $Cs_2Au_2Cl_6$_1 and $Cs_2Au_2Cl_6$_3 samples.

the experiment: first peaks, *a* at ∼4 eV and *b* at ∼6 eV, are nicely reproduced and mainly have a Au 5d character, shoulder *c* at ∼8 eV mainly has a Au 5d character, peak *d* at ∼10 eV has a contribution of Au 5d with Cs 5p states, and peak *e* at ∼12 eV mainly has a Cs 5p character. Finally, the peak *f* at ∼16 eV has a contribution of Cl 3s with some Au 4f + 5d states. Figure 6b−d displays the computed VB-XPS for $Cs_2Au_2X_6$ for X = Br, I, and Cl, respectively. The results of simulated XPS using HSE06 + SOC compared with the experiment provide us more confidence in the method used in this work. We are aware that HSE06 + GW could provide more precise prediction of the band gaps but it misses the spin−orbit corrections needed to explain the observed XPS spectra. For this reason, we argue that SCAN/HSE06 + SOC provides a good quality of predictions that can be safely applied to similar systems.

Morphological and chemical analyses of the $Cs_2Au_2Cl_6$ samples were performed using a scanning electron microscope (SEM) equipped with an energy-dispersive X-ray spectroscopy (EDS) detector. The stoichiometric elemental composition is also corroborated by EDS elemental mapping that was followed by quantification of the desired features. EDS-SEM elemental maps of $Cs_2Au_2Cl_6$_2 are presented in Figure 7: the Cs, Au, and Cl maps seem identical, and a uniform elemental composition was observed for all the crystals in the image. Elemental ratios of Cs/Au/Cl, (retrieved from the quantification results) measured at different spots on the sample, give an average of 21.88 (SD 0.70)/17.47 (SD 0.61)/60.65 (SD 1.08), which is in excellent agreement with the expected stoichiometry of $Cs_2Au_2Cl_6$ (see Table 3 for full details).

Furthermore, cathodoluminescence (CL) measurements were performed. CL emission spectra of $Cs_2Au_2Cl_6$_2 presented in Figure 8 show a wide emission centered around 900 nm (∼1.38 eV) with an FWHM of ∼185 nm (0.3 eV), in good agreement with the band gap of 1.4 eV as predicted by DFT calculation above.

The photocatalytic activity of $Cs_2Au_2Cl_6$ was evaluated by photodegradation of toluene in the gas phase both under UV (λ_{max} = 375 nm, I = 9.2 mW·cm^{-2}) and vis (λ_{max} = 415 nm, I = 0.4 mW·cm^{-2}) LED irradiation after 60 min. Based on XRD analysis, two of the most promising samples were selected for the photocatalytic tests: $Cs_2Au_2Cl_6$_5 and $Cs_2Au_2Cl_6$_2 that exhibited the highest crystallinity and presented the best purity, respectively. Toluene, a volatile organic compound (VOC) widely distributed in the environment, was used as a model air

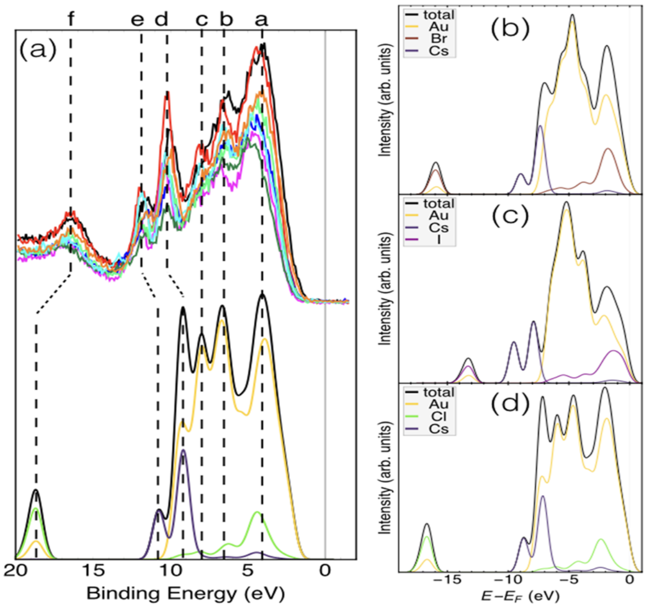

Figure 6. Theory versus experiment, (a) VB-XPS spectra measured at $h\nu$ = 1486.6 eV (upper panel) compared with the HSE06 + SOC-simulated XPS spectrum (lower panel) for $Cs_2Au^IAu^{III}Cl_6$ with symmetry *I4/mmm*. HSE06 + SOC-simulated XPS spectra at $h\nu$ = 1486.6 eV for $Cs_2Au^IAu^{III}X_6$ with symmetry *I4/mmm* for (b) X = Br, (c) X = I, and (d) X = Cl. Notice that (d) and lower panel (a) are the same.

pollutant. The kinetics of toluene degradation in the presence of $Cs_2Au_2Cl_6$ photocatalysts are shown in Figure 9. The blank test showed that toluene concentration decreased by about 5% after 60 min, indicating that the degradation of toluene without the photocatalyst can be neglected. It could be seen that the $Cs_2Au_2Cl_6$ samples have shown photoactivity in toluene degradation in the gas phase. Toluene removal efficiency under ultraviolet light irradiation reached approximately 29 and 32% for $Cs_2Au_2Cl_6$_5 and $Cs_2Au_2Cl_6$_2, respectively. Meanwhile, the efficiency of toluene photodegradation under visible light was about 35 and 58% in the presence of $Cs_2Au_2Cl_6$_5 and $Cs_2Au_2Cl_6$_2, respectively. It indicates that $Cs_2Au_2Cl_6$ can absorb visible light effectively due to its narrow band gap and is in good agreement with theoretical calculations. Moreover, it may be suggested that gold impurities determined by XRD, SEM (see Supporting Information, Figure S3), and XPS analysis in the $Cs_2Au_2Cl_6$_5 photocatalyst can aggregate and act as recombination centers for photogenerated charge carriers, leading to lower performance.[45,46] Therefore, the higher photoefficiency of $Cs_2Au_2Cl_6$_2 is potentially due to the higher purity of this photocatalyst (i.e., the absence of gold nanoparticles).

Furthermore, it is important to evaluate the stability of the photocatalyst for practical applications. The experimental stability of $Cs_2Au_2Cl_6$ was tested after exposure to various conditions (high temperature, long time storage, irradiation in the gas and aqueous phase) and analyzed by pXRD as shown in Figure S6. XRD patterns confirmed structural stability of $Cs_2Au_2Cl_6$ after heating at 100 °C in air for 72 h (Figure S6a) and 2 years of storage at room temperature in the dark (Figure S6b). Importantly, $Cs_2Au_2Cl_6$ exhibited excellent stability after photocatalytic tests of toluene degradation in the gas phase under UV irradiation (Figure S6c). Meanwhile, XRD analysis showed decomposition of $Cs_2Au_2Cl_6$ into elemental gold particles (Figure S6d) after additional photocatalytic tests toward degradation of phenol in the aqueous phase under UV irradiation. It may indicate photocorrosion of $Cs_2Au_2Cl_6$ as a result of gold ion diffusion and photoreduction to metallic Au in the aqueous medium. A similar degradation pathway was reported by Bekenstein et al.[47] who identified silver diffusion,

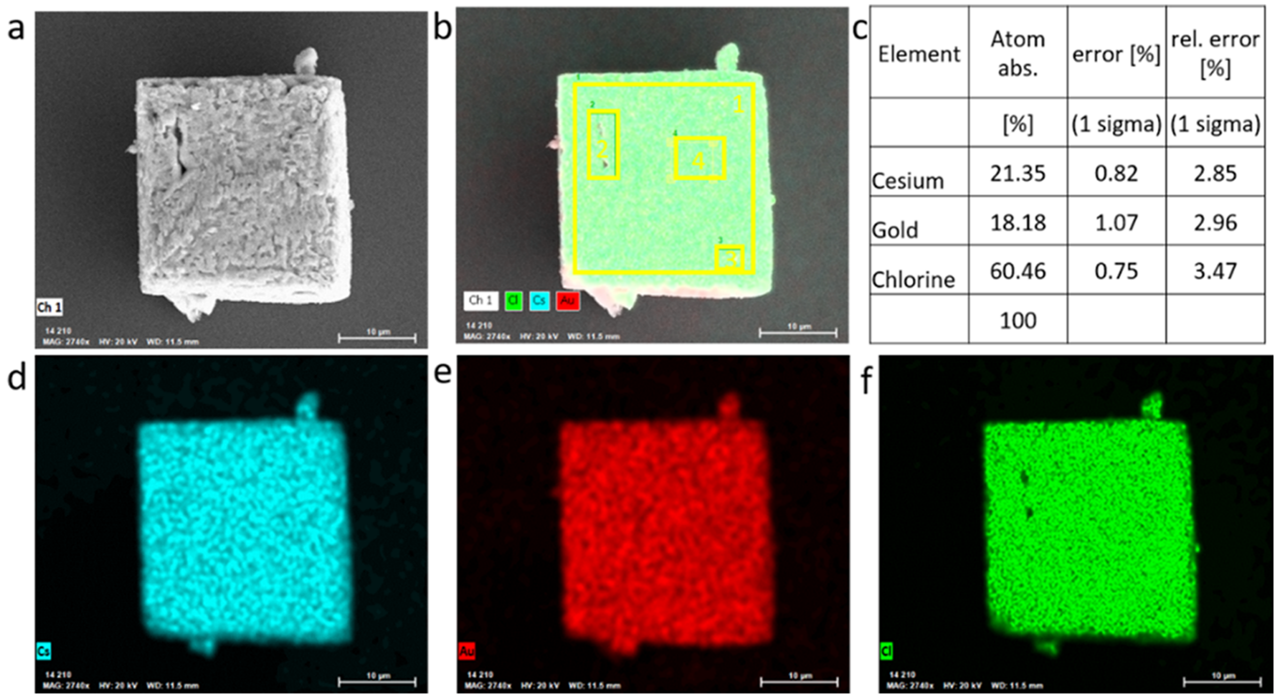

Element	Atom abs.	error [%]	rel. error [%]
	[%]	(1 sigma)	(1 sigma)
Cesium	21.35	0.82	2.85
Gold	18.18	1.07	2.96
Chlorine	60.46	0.75	3.47
	100		

Figure 7. EDS analysis. (a, b) SEM image of sample $Cs_2Au_2Cl_6$_2 with the corresponding elemental map. (c) EDS spectra of area 1 marked in yellow in (b). (d−f) EDS elemental maps of Cs, Au, and Cl, respectively.

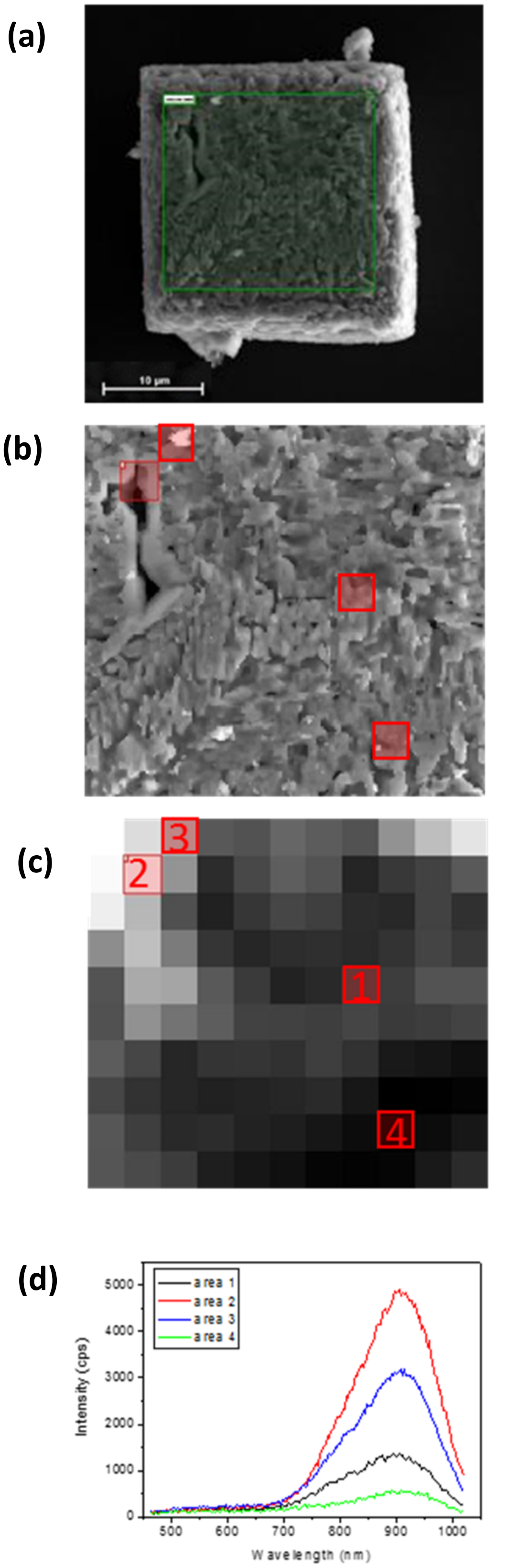

Figure 8. Cathodoluminescence SEM. (a, b) SEM images of sample $Cs_2Au_2Cl_6$_2. (c) Pixelated intensity CL image. (d) CL spectra of different areas on the sample as marked in red in (c).

reduction, and coalescence as the main reason of structural instability of $Cs_2AgBiBr_6$ NCs.[47]

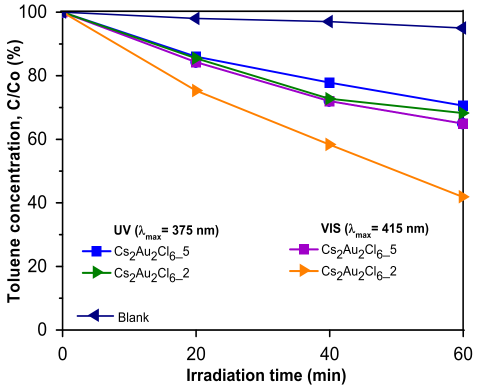

Figure 9. Efficiency of toluene photodegradation as a function of irradiation under UV (λ_{max} = 375 nm) and vis (λ_{max} = 415 nm) LED irradiation over $Cs_2Au_2Cl_6$_5 and $Cs_2Au_2Cl_6$_2 samples.

■ CONCLUSIONS

Using systematic first-principles calculations and material screening processes that considered $Cs_2Au_2X_6$ (X = Cl, Br, and I) crystal structures with *I*4/*mmm* (no. 139) and *Pm*-3*m* (no. 221) symmetries allowed us to identify the most stable structures for these double perovskites that belong to the *I*4/*mmm* symmetry, making them promising materials in photocatalytic reactions. By SCAN meta-GGA prediction of the EOS and computed phonon dispersions, we found that tetragonal perovskites $Cs_2Au^{I}Au^{III}X_6$ with symmetry *I*4/*mmm* show good phase stability. With use of more accurate HSE06 + SOC calculations, we classified $Cs_2Au^{I}Au^{III}X_6$ perovskite materials in terms of electronic structure features. In addition, we found that tetragonal $Cs_2Au^{I}Au^{III}X_6$ molecules with symmetry I4/mmm present an indirect band gap with values equal to 1.10, 1.15, and 1.40 eV for $Cs_2Au^{I}Au^{III}I_6$, $Cs_2Au^{I}Au^{III}Br_6$, and $Cs_2Au^{I}Au^{III}Cl_6$ perovskites, respectively. The Goldschmidt tolerance factor suggests that these materials are stable in agreement with our DFT calculations. Following these theoretical and numerical findings, we developed a novel one-step preparation route of double perovskite $Cs_2Au_2Cl_6$ using a combination of monovalent and trivalent gold precursors under solvothermal or reflux conditions at a relatively low temperature. Detailed physicochemical characterization of as-obtained $Cs_2Au_2Cl_6$ confirmed our theoretical calculations. In addition, the structure, morphology, and surface properties of $Cs_2Au^{I}Au^{III}Cl_6$ are dependent strongly on synthesis parameters. Furthermore, it was found that double perovskite $Cs_2Au_2Cl_6$ exhibits high efficiency in a photocatalytic toluene degradation reaction under visible light irradiation (λ_{max} = 415 nm). The HSE06 + SOC simulations of the VB-XPS for $Cs_2Au^{I}Au^{III}Cl_6$ replicate nicely the observed spectrum, providing strong evidence of the reliability of the obtained results for the other perovskites $Cs_2Au^{I}Au^{III}X_6$, X = Br, I. These results stress the importance of including spin−orbit corrections on the calculations of this type of double perovskite. Our study may provide useful guide for designing and fabrication of efficient gold-based double halide perovskites for photocatalytic and solar cell applications.

■ ASSOCIATED CONTENT

SI Supporting Information

The Supporting Information is available free of charge at https://pubs.acs.org/doi/10.1021/acs.jpcc.0c07782.

SCAN-computed EOS; SCAN-computed crystallographic data; SCAN-computed PDOS; XRD patterns; EDX elemental analysis; cathodoluminescence SEM images; DRS UV−vis spectrum (PDF)

AUTHOR INFORMATION

Corresponding Authors

Dan Oron − *Department of Physics of Complex Systems, Weizmann Institute of Science, Rehovot 76100, Israel;* orcid.org/0000-0003-1582-8532; Email: dan.oron@weizmann.ac.il

Adriana Zaleska-Medynska − *Department of Environmental Technology, Faculty of Chemistry, University of Gdansk, Gdansk 80-308, Poland;* orcid.org/0000-0003-3817-296X; Email: adriana.zaleska-medynska@ug.edu.pl

Authors

Beata Bajorowicz − *Department of Environmental Technology, Faculty of Chemistry, University of Gdansk, Gdansk 80-308, Poland;* orcid.org/0000-0001-8427-5981

Alicja Mikolajczyk − *Laboratory of Environmental Chemometrics, Faculty of Chemistry, University of Gdansk, Gdansk 80-308, Poland*

Henry P. Pinto − *CompNano Group, School of Physical Sciences and Nanotechnology, Yachay Tech University, Urcuqui 100119, Ecuador*

Magdalena Miodyńska − *Department of Environmental Technology, Faculty of Chemistry, University of Gdansk, Gdansk 80-308, Poland*

Wojciech Lisowski − *Institute of Physical Chemistry, Polish Academy of Sciences, Warsaw 01-224, Poland*

Tomasz Klimczuk − *Department of Solid State Physics, Faculty of Applied Physics and Mathematics, Gdansk University of Technology, Gdansk 80-233, Poland;* orcid.org/0000-0002-7089-4631

Ifat Kaplan-Ashiri − *Department of Chemical Research Support, Weizmann Institute of Science, Rehovot 76132701, Israel*

Miri Kazes − *Department of Physics of Complex Systems, Weizmann Institute of Science, Rehovot 76100, Israel;* orcid.org/0000-0003-0796-3945

Complete contact information is available at: https://pubs.acs.org/10.1021/acs.jpcc.0c07782

Author Contributions

The manuscript was written through the contributions of all of the authors. Authors B.B. and A.M. contributed equally to this work. All of the authors have given approval to the final version of the manuscript.

Notes

The authors declare no competing financial interest.

ACKNOWLEDGMENTS

This research was financially supported by the National Science Centre, Poland (2016/23/B/ST8/03336 and 2017/24/U/ST5/00056) and supported by the Foundation for Polish Science (FNP) (START 1.2019/ START 58.2019) and BMN No. 538-8620-B244-18. H.P.P. acknowledges the generous computer resources from the Center for Scientific Computing (CSC) in Espoo, Finland supported by the HPC-Europa3 (grant HPC17WE2EY).

REFERENCES

(1) Yin, W.-J.; Weng, B.; Ge, J.; Sun, Q.; Li, Z.; Yan, Y. 35. *Energy Environ. Sci.* **2019**, *12*, 442−462.

(2) Maughan, A. E.; Ganose, A. M.; Scanlon, D. O.; Neilson, J. R. Perspectives and Design Principles of Vacancy-Ordered Double Perovskite Halide Semiconductors. *Chem. Mater.* **2019**, *31*, 1184−1195.

(3) Lee, J.-W.; Hsieh, Y.-T.; De Marco, N.; Bae, S.-H.; Han, Q.; Yang, Y. Halide Perovskites for Tandem Solar Cells. *J. Phys. Chem. Lett.* **2017**, *8*, 1999−2011.

(4) Jishi, R. A.; Ta, O. B.; Sharif, A. A. Modeling of Lead Halide Perovskites for Photovoltaic Applications. *J. Phys. Chem. C* **2014**, *118*, 28344−28349.

(5) Manser, J. S.; Christians, J. A.; Kamat, P. V. Intriguing Optoelectronic Properties of Metal Halide Perovskites. *Chem. Rev.* **2016**, *116*, 12956−13008.

(6) Xu, X.; Zhong, Y.; Shao, Z. Double perovskites in catalysis, electrocatalysis, and photo(electro)catalysis. *Trends Chem.* **2019**, *1*, 410−424.

(7) Zhao, X.-G.; Yang, J.-H.; Fu, Y.; Yang, D.; Xu, Q.; Yu, L.; Wei, S.-H.; Zhang, L. Design of Lead-Free Inorganic Halide Perovskites for Solar Cells via Cation-Transmutation. *J. Am. Chem. Soc.* **2017**, *139*, 2630−2638.

(8) Hoefler, S. F.; Trimmel, G.; Rath, T. Progress on lead-free metal halide perovskites for photovoltaic applications: a review. *Monatsh. Chem.* **2017**, *148*, 795−826.

(9) Retuerto, M.; Emge, T.; Hadermann, J.; Stephens, P. W.; Li, M. R.; Yin, Z. P.; Croft, M.; Ignatov, A.; Zhang, S. J.; Yuan, Z.; Jin, C.; Simonson, J. W.; Aronson, M. C.; Pan, A.; Basov, D. N.; Kotliar, G.; Greenblatt, M. Synthesis and properties of charge-ordered thallium halide perovskites, $CsTl1^{+}{}_{0.5}Tl^{3+}{}_{0.5}X_3$ (X = F, Cl) : Theoretical Precursors for Superconductivity? *Chem. Mater.* **2013**, *25*, 4071−4079.

(10) Debbichi, L.; Lee, S.; Cho, H.; Rappe, A. M.; Hong, K. H.; Jang, M. S.; Kim, H. Mixed Valence Perovskite $Cs_2Au_2I_6$: A Potential Material for Thin-Film Pb-Free Photovoltaic Cells with Ultrahigh Efficiency. *Adv. Mater.* **2018**, *30*, 1707001.

(11) Castro-Castro, L. M.; Guloy, A. M. Organic−Based Layered Perovskites of Mixed−Valent Gold(I)/Gold(III) Iodides. *Angew. Chem., Int. Ed.* **2003**, *42*, 2771−2774.

(12) Wells, H. L. Some complex chloride containing gold. *Am. J. Sci.* **1922**, *3*, 315−326.

(13) Elliott, N.; Pauling, L. The Crystal Structure of Cesium Aurous Auric Chloride, $Cs_2AuAuCl_6$, and Cesium Argentous Auric Chloride, $Cs_2AgAuCl_6$. *J. Am. Chem. Soc.* **1938**, *60*, 1846−1851.

(14) Keller, R.; Fenner, J.; Holzapfel, W. B. The resistivity of mixed valence compound $Cs_2Au_2Cl_6$ at high pressure and low temperatures. *Mater. Res. Bull.* **1974**, *9*, 1363−1369.

(15) Matsushita, N.; Ahsbahs, H.; Hafner, S. S.; Kojima, N. Single crystal X-ray diffraction study of a mixed-valence gold compound, $Cs_2Au^{I}Au^{III}Cl_6$ under high pressures up to 18 GPa: Pressure-induced phase transition coupled with gold valence transition. *J. Solid State Chem.* **2007**, *180*, 1353−1364.

(16) Brauer, G.; Sleater, G. Preparation of mixed valent aurate halides. *J. Less-Common Met.* **1970**, *21*, 283−291.

(17) Riggs, S. C.; Shapiro, M. C.; Corredor, F.; Geballe, T. H.; Fisher, I. R.; McCandless, G. T.; Chan, J. Y. *Single crystal growth* by *self-flux method* of the *mixed valence gold* halides $Cs_2[Au^{I}X_2][Au^{III}X_4]$ (*X=Br,I*). *J. Cryst. Growth* **2012**, *355*, 13−16.

(18) Kresse, G.; Furthmüller, J. Efficient iterative schemes for ab initio total-energy calculations using a plane-wave basis set. *Phys. Rev. B* **1996**, *54*, 11169−11186.

(19) Kresse, G.; Furthmüller, J. Efficiency of ab-initio total energy calculations for metals and semiconductors using a plane-wave basis set. *Comput. Mater. Sci.* **1996**, *6*, 15−50.

(20) Kresse, G.; Joubert, D. From ultrasoft pseudopotentials to the projector augmented-wave method. *Phys. Rev. B* **1999**, *59*, 1758−1775.

(21) Sun, J.; Ruzsinszky, A.; Perdew, J. P. Strongly Constrained and Appropriately Normed Semilocal Density Functional. *Phys. Rev. Lett.* **2015**, *115*, No. 036402.

(22) Hinuma, Y.; Hayashi, H.; Kumagai, Y.; Tanaka, I.; Oba, F. Comparison of approximations in density functional theory calculations: Energetics and structure of binary oxides. *Phys. Rev. B* **2017**, *96*, No. 094102.

(23) Heyd, J.; Scuseria, G. E.; Ernzerhof, M. Hybrid functionals based on a screened Coulomb potential. *J. Chem. Phys.* **2003**, *118*, 8207−8215.

(24) Krukau, A. V.; Vydrov, O. A.; Izmaylov, A. F.; Scuseria, G. E. Influence of the exchange screening parameter on the performance of screened hybrid functionals. *J. Chem. Phys.* **2006**, *125*, 224106−224111.

(25) Sun, J.; Remsing, R. C.; Zhang, Y.; Sun, Z.; Ruzsinszky, A.; Peng, H.; et al. Accurate first-principles structures and energies of diversely bonded systems from an efficient density functional. *Nat. Chem.* **2016**, *8*, 831−836.

(26) Zhang, Y.; Sun, J.; Perdew, J. P.; Wu, X. Comparative first-principles studies of prototypical ferroelectric materials by LDA, GGA, and SCAN meta-GGA. *Phys. Rev. B* **2017**, *96*, No. 035143.

(27) Shahi, C.; Sun, J.; Perdew, J. P. Accurate critical pressures for structural phase transitions of group IV, III−V, and II−VI compounds from the SCAN density functional. *Phys. Rev. B* **2018**, *97*, No. 094111.

(28) Zhang, Y.; Kitchaev, D. A.; Yang, J.; Chen, T.; Dacek, S. T.; Sarmiento-Pérez, R. A.; et al. Efficient first-principles prediction of solid stability: towards chemical accuracy. *npj Comput. Mater.* **2018**, *4*, 9.

(29) Mathematical physics in theoretical chemistry, *Developments in physical & theoretical chemistry* Blinder, S.M.; House, J.E., Eds.; 1st edition, Elsevier, 2019.

(30) Togo, A.; Tanaka, I. First principles phonon calculations in materials science. *Scr. Mater.* **2015**, *108*, 1−5.

(31) Goldschmidt, V. M. Die gesetze der krystallochemie. *Naturwissenschaften* **1926**, *14*, 477−485.

(32) Shannon, R. D. Revised effective ionic radii and systematic studies of interatomic distances in halides and chalcogenides. *Acta Crystallogr., Sect. A: Found. Crystallogr.* **1976**, *32*, 751−767.

(33) Bartel, C. J.; Sutton, C.; Goldsmith, B. R.; Ouyang, R.; Musgrave, C. B.; Ghiringhelli, L. M.; Scheffler, M. New tolerance factor to predict the stability of perovskite oxides and halides. *Sci. Adv.* **2019**, *5*, eaav0693.

(34) Balachandran, P. V.; Emery, A. A.; Gubernatis, J. E.; Lookman, T.; Wolverton, C.; Zunger, A. Predictions of new ABO_3 perovskite compounds by combining machine learning and density functional theory. *Phys. Rev. Mater.* **2018**, *2*, 043802.

(35) Pilania, G.; Balachandran, P. V.; Kim, C.; Lookman, T. Finding new perovskite halides via machine learning. *Front. Mater.* **2016**, *3*, 19.

(36) Pilania, G.; Balachandran, P. V.; Gubernatis, J. E.; Lookman, T. Classification of ABO_3 perovskite solids: A machine learning study. *Acta Cryst.* **2015**, *71*, 507−513.

(37) Matsushita, N.; Ahsbahs, H.; Hafner, S. S.; Kojima, N. Crystal Structure of Mixed-Valence Gold Compound, $Cs_2Au^IAu^{III}Cl_6$ up to 18 GPa. *Rev. High Pressure Sci. Technol.* **1998**, *7*, 329−331.

(38) Kangsabanik, J.; Ghorui, S.; Aslam, M.; Alam, A. Optoelectronic Properties and Defect Physics of Lead-free Photovoltaic Absorbers $Cs_2Au^IAu^{III}X_6$ (X = I, Br). *Phys. Rev. Applied* **2020**, *13*, 014005.

(39) Eijndhoven, J. C. M. T.-V.; Verschoor, G. C. Redetermination of the crystal structure of $Cs_2AuAuCl_6$. *Mater. Res. Bull.* **1974**, *9*, 1667−1670.

(40) Ghosh, B.; Febriansyah, B.; Harikesh, P. C.; Koh, T. M.; Hadke, S.; Wong, L. H.; England, J.; Mhaisalkar, S. G.; Mathews, N. Direct Band Gap Mixed-Valence Organic−inorganic Gold Perovskite as Visible Light Absorbers. *Chem. Mater.* **2020**, *32*, 6318−6325.

(41) Naumkin, A. V.; Kraut-Vass, A.; Gaarenstroom, S. W.; Powell, C. J. *NIST X-ray Photoelectron Spectroscopy Database 20*, Version 4.1, National Institute of Standards and Technology, Gaithersburg, http://srdata.nist.gov/xps , 2012.

(42) Son, J.-Y.; Mizokawa, T.; Quilty, J. W.; Takubo, K.; Ikeda, K.; Kojima, N. Photoinduced valence transition in gold complexes $Cs_2Au_2X_6$ (X = Cl and Br) probed by x-ray photoemission spectroscopy. *Phys. Rev. B* **2005**, *72*, 235105.

(43) Kitagawa, H.; Kojima, N.; Nakajima, T. Studies of Mixed-valence States in Three-dimensional Halogen-bridged Gold Compounds, $Cs_2Au^IAu^{III}X_6$, (X=Cl, Br or I). Part 2. X-Ray Photoelectron Spectroscopic Study. *J. Chem. Soc., Dalton Trans.* **1991**, *11*, 3121−3125.

(44) Park, E. D.; Lee, J. S. Effects of Pretreatment Conditions on CO Oxidation over Supported Au Catalysts. *J. Catal.* **1999**, *186*, 1−11.

(45) Cacovich, S.; Ciná, L.; Matteocci, F.; Divitini, G.; Midgley, P. A.; Di Carlo, A.; Ducati, C. Gold and iodine diffusion in large area perovskite solar cells under illumination. *Nanoscale* **2017**, *9*, 4700−4706.

(46) Li, H.; Bian, Z.; Zhu, J.; Huo, Y.; Li, H.; Lu, Y. Mesoporous Au/TiO_2 Nanocomposites with Enhanced Photocatalytic Activity. *J. Am. Chem. Soc.* **2007**, *129*, 4538−4539.

(47) Bekenstein, Y.; Dahl, J. C.; Huang, J.; Osowiecki, W. T.; Swabeck, J. K.; Chan, E. M.; Yang, P.; Alivisatos, A. P. The Making and Breaking of Lead-Free Double Perovskite Nanocrystals of Cesium Silver-Bismuth Halide Compositions. *Nano Lett.* **2018**, *18*, 3502−3508.

https://dx.doi.org/10.1021/acs.jpcc.0c07782